

Electronic Supplementary Information for A Self-circulating Pathway for Oxygen Evolution Reaction

Bohan Deng,^{‡a} Guangqiang Yu,^{‡b} Wei Zhao,^a Yuanzheng Long,^a Cheng Yang,^a Peng Du,^c Xian He,^c Zhuting Zhang,^a Kai Huang,^{*c} Xibo Li ^{*b} and Hui Wu ^{*a}

^aState Key Lab of New Ceramics and Fine Processing, School of Materials Science and Engineering, Tsinghua University; Beijing, 100084, China

^bSiyuan Laboratory, Guangzhou Key Laboratory of Vacuum Coating Technologies and New Energy Materials, Guangdong Provincial Engineering Technology Research Center of Vacuum Coating Technologies and New Energy Materials, Department of Physics, Jinan University; Guangzhou, Guangdong, 510632, China

^cState Key Laboratory of Information Photonics and Optical Communications & School of Science, Beijing University of Posts and Telecommunications; Beijing, 100876, China

*E-mail: huiwu@tsinghua.edu.cn (H.W.), lixibo@jnu.edu.cn (X.L.), huang-kai@bupt.edu.cn (K.H.)

[‡]These authors contributed equally to this work.

content

Experimental Section.....	2
Supplementary Note 1: Calculations of standard OER potentials E^0 vs RHE at arbitrary temperature	5
Supplementary Note 2: Detailed information for DFT calculation	7
Supplementary Note 3: Calculations on the overall energy efficiency	10
Supplementary Figures	11
Supplementary Tables	34
Supplementary References	39

Experimental Section

Materials

Nickel nitrate hexahydrate ($\text{Ni}(\text{NO}_3)_2 \cdot 6\text{H}_2\text{O}$, GR, >99%) was purchased from Aladdin. Potassium hydroxide (KOH, 99.99% metals basis, except sodium) was purchased from Macklin. Hydrochloric acid (HCl, 37%) was purchased from Sinopharm. Acetone (CH_3COCH_3 , AR, >99.5%) was purchased from Aladdin. ^{18}O -labelled water (H_2^{18}O , >98% ^{18}O) was purchased from China isotope Co. Ltd. Nickel foam (1mm thick) was purchased from Lizhiyuan Co. Ltd.

Preparation of $\text{Ni}(\text{OH})_2/\text{NF}$ electrodes

$\text{Ni}(\text{OH})_2/\text{NF}$ electrodes were prepared using an electroplating method. Ni foam substrates were cut into 1 cm \times 1.5 cm pieces and thoroughly washed in acetone and 1M hydrochloric acid for 15 min by ultrasonication to remove impurities and the surface oxide layer, then washed with deionized water. A deposition solution of 0.5M $\text{Ni}(\text{NO}_3)_2$ dissolved in deionized water was used for the electroplating process. Each Ni foam substrate was dipped into the deposition solution with a plating area of 1 cm \times 1 cm and the remaining part was used as the electrical contact. The electrochemical deposition experiment was conducted via chronopotentiometry mode with a cathodic current of 20 mA for 30 min. After deposition, the electrode was washed thoroughly with deionized water, then aged in a 12 mol kg $^{-1}$ KOH aqueous solution at 120 °C for 1h.

Catalyst characterizations

Scanning electron microscopy (SEM) images were taken by a Zeiss microscope (MERLIN VP Compact) operated at 15 kV. TEM and HR-TEM images were taken by a 2100F transmission electron microscope operated at 200 kV. X-ray diffraction analysis was performed by a D/max 2500V diffractometer in reflection mode at 40 kV and 150 mA with a scanning speed of 8 ° min $^{-1}$. Raman spectra were collected using a confocal Raman microscope (LabRAM HR Evolution, HORIBA Jobin Yvon) with a wavelength of 532 nm and a power of 5 mW at the objective. X-ray photoelectron spectra were collected using a Thermo Fisher spectrometer (Escalab 250Xi) equipped with an Al K α radiation source (1487.6 eV) and hemispherical analyzer with a pass energy of 30.0 eV and energy step size of 0.05 eV. All the XPS spectra were corrected by C 1s peak of 284.8 eV and fitted using XPSPEAK41 software with Shirley backgrounds and Gaussian-Lorentzian functions. The Fe content was measured by an inductively coupled plasma optical emission spectrometer (IRIS Intrepid II XSP, Thermo Fisher).

RHE Calibration of reference electrode

A Hg/HgO/1M KOH reference electrode was used as reference electrode in all measurements with three-electrode system. It was calibrated with respect to reversible hydrogen electrode (RHE) using a three-electrode system with two cleaned Pt electrodes as the working and counter electrodes. Before calibration, the Pt electrodes were cleaned by conducting CV between -2 V and +2 V at 100 mV s $^{-1}$ for 2 hours in 1 M H_2SO_4 . The electrolyte was pre-purged and saturated with

high-purity H₂, and H₂ was constantly bubbled over the working electrode during the calibration. Linear sweep voltammetry (LSV) was conducted at a scan rate of 0.1 mV s⁻¹, and the potential at zero current point was taken to be the thermodynamic potential (vs. Hg/HgO/1M KOH) for the hydrogen electrode reactions, as shown in Fig. S9. For example, at 25 °C, the zero current point was at -1.034 V, and therefore E (RHE) = E (Hg/HgO/1M KOH) + 1.034 V. The calibration was conducted at temperatures ranging from 25 °C ~120 °C and the results were summarized in Table S2.

Electrochemical measurement

All electrochemical tests were carried out on an electrochemical workstation (PGSTAT204, Autolab). Except otherwise noted, the electrolyte used in electrochemical tests was 12 mol kg⁻¹ KOH. In the three-electrode system, Ni(OH)₂/NF electrode was used as the working electrode, along with a Ni foam counter electrode and a Hg/HgO/1M KOH reference electrode. To keep the KOH concentration and the temperature of the Hg/HgO/1M KOH reference electrode stable during the test, two salt bridges were used and the solution in the outer salt bridge was replaced with fresh 1M KOH every 30 min. A hot stage with a thermocouple was used to maintain the electrolyte at set temperatures. Cyclic voltammetry (CV) was conducted with a scan rate of 1 mV s⁻¹. The steady-state water oxidation current was collected by recording the stable current at the end of the 5-min chronoamperometry program. IR corrected by 90% of the solution resistance was employed to eliminate the effect of solution resistance. The resistance was measured by electrochemical impedance spectroscopy (EIS) with high frequency of 100 kHz and low frequency of 0.01 Hz at 0.3 V vs Hg/HgO. The electrochemically active surface area (ECSA) was fitted by cyclic voltammetry curves in the potential range of -0.3 ~ -0.2 V vs Hg/HgO at 1 ~ 100 mV s⁻¹. For the stability test, chronopotentiometry was applied at the current of 10 mA cm⁻² for 15h. To make a commercial Ir/C catalyst sample, 5 mg 20% Ir/C (Premetek) was dispersed into a mixture solution (800 μL of ethanol, 150 μL of ultrapure water, and 50 μL of 5wt% Nafion solution). The mixture was sonicated for 10 min to make a uniform catalyst ink. Subsequently, 50 μL of catalyst ink was uniformly loaded onto carbon paper (1 cm × 0.5 cm), maintaining the loading of Ir element at 100 μg cm⁻².

Faradaic efficiency calculation

To determine the Faradaic efficiency of water splitting, an H-type cell was used to collect the generated oxygen and hydrogen separately via drainage gas gathering method. As the gases were generated at high temperatures, the volume of the generated gases was recorded after they cooled down to 25 °C and the partial pressure of water vapor (3.167 KPa at 25 °C) was subtracted when calculating the amount of generated gases. The Faradaic efficiency can be calculated as:

$$FE(\%) = \frac{V_{gas} \cdot nF}{V_m \cdot it} \times 100\%$$

Investigation on the isotope behavior of oxygen

The ^{18}O -labeled KOH electrolyte was prepared with KOH and H_2^{18}O (>98% ^{18}O). To prepare a labeled $\text{Ni}(\text{OH})_2/\text{NF}$ electrode, a $\text{Ni}(\text{NO}_3)_2$ solution prepared with H_2^{18}O was used for the electroplating process. Prior to the thermal decomposition experiment, the labeled $\text{Ni}(\text{OH})_2/\text{NF}$ electrode was charged to the NiOOH state in the ^{18}O -labeled KOH electrolyte and then washed with unlabeled water to remove the ^{18}O -labeled KOH electrolyte. In contrast, the unlabeled $\text{Ni}(\text{OH})_2/\text{NF}$ electrode was charged in unlabeled KOH electrolyte. The oxygen generated from the thermal decomposition process was analyzed using an on-line mass spectrometer system (PM-QMS, Shanghai Pro-tech Co. Ltd.). It is noted that the on-line acquisition mode requires a relatively large amount of gas sample, so actually the gas sample for detection is a mixture of the generated O_2 and air.

Evaluation of the thermal decomposition rate of NiOOH

The thermal decomposition rate of NiOOH was evaluated using an electrochemical method proposed by Dotan *et al.* First, the $\text{Ni}(\text{OH})_2/\text{NF}$ electrode was discharged at 10 mA cm^{-2} to a cutoff potential of 0 V vs Hg/HgO, then charged at 10 mA cm^{-2} to a cutoff potential of 0.4 V vs Hg/HgO under room temperature. It is noted that OER would not occur under 0.4 V vs Hg/HgO, as shown in Fig. 2c, so the charge entirely came from the formation of NiOOH from $\text{Ni}(\text{OH})_2$. After the charge to 0.4 V vs Hg/HgO was finished, the $\text{Ni}(\text{OH})_2/\text{NF}$ electrode was immersed into a hot 12 mol kg^{-1} KOH solution for a certain amount of time. The electrode was then charged again at 10 mA cm^{-2} to the same cutoff potential of 0.4 V vs Hg/HgO to recover the previous state. The charge quantity corresponds to the amount of $\text{Ni}(\text{OH})_2$ generated from the thermal decomposition of NiOOH during the hot solution treatment, so the thermal decomposition density of NiOOH is given by $Q = j_{\text{charge}} * t$. This procedure was repeated five times at each data point in Fig. 4a, and the error bars represent the standard deviation.

Computational methods

The density functional theory (DFT) calculations were performed by using the Vienna ab-initio simulation package (VASP)^{1,2}. The electron exchange-correlation potential was conducted by Perdew-Burke-Ernzerhof (PBE) functional of generalized gradient approximation (GGA)³. The applied energy cutoff was 400 eV for the plane-wave basis set. The Gamma-center Monkhorst-Pack k-point mesh⁴ with a distance of $0.03/\text{\AA}$ was used for the structural relaxations. All the calculated results were considered to achieve a good convergence until the force on each atom is less than $0.05 \text{ eV}/\text{\AA}$. The electron energy convergence value between two consecutive steps was set to be $1 \times 10^{-5} \text{ eV}$. The dispersion correction was realized by DFT + D3 method^{5,6}. The PBE + U method was used to accurately describe the Ni 3d electron states with $U_{\text{eff}} = 5.5 \text{ eV}$ ^{7,8}. A vacuum space larger than 15 \AA is applied to each slab.

Supplementary Note 1: Calculations of standard OER potentials E^0 vs RHE at arbitrary temperature

According to the definition of RHE, the standard OER potential is equal to the standard potential for water splitting (E^0), which is 1.229 V at $T=298.15$ K. This well-known figure is widely used in water electrolysis research when calculating overpotentials, even if the experiment was performed at another temperature⁹⁻¹¹. However, E^0 changes with temperature, and this effect is not negligible when the reaction proceeds at a much higher temperature. The standard potentials for water splitting at arbitrary temperatures $E^0(T)$ are described by equations as follows:

$$E^0(T) = \frac{\Delta G_{r,H_2O}^0(T)}{zF} \quad (1)$$

where $\Delta G_{r,H_2O}^0(T)$ denotes the standard Gibbs free energy of water splitting reaction ($H_2O(l) \rightarrow H_2(g) + 1/2 O_2(g)$) at temperature T , which can be obtained by:

$$\Delta G_{r,H_2O}^0(T) = -G_{H_2O(l)}^0(T) + G_{H_2(g)}^0(T) + \frac{1}{2}G_{O_2(g)}^0(T) \quad (2)$$

According to the model developed by Carter et al.¹², the standard Gibbs free energies of molecular species can be described as follows:

$$G_i^0(T) = E_i^{DFT} + ZPE_i^{DFT} + [H_i^0(T) - H_i^0(0 K) - TS_i^0(T)] \quad (3)$$

where i denotes $H_2O(l)$, $H_2(g)$ or $O_2(g)$, E_i^{DFT} is the species' DFT total energy at 0 K, ZPE_i^{DFT} is the species' zero-point vibrational energy from DFT, $H_i^0(T)$ and $S_i^0(T)$ are the species' standard enthalpy and entropy at T , respectively. Especially, for $T=T_r=298.15$ K:

$$G_i^0(T_r) = E_i^{DFT} + ZPE_i^{DFT} + [H_i^0(T_r) - H_i^0(0 K) - T_r S_i^0(T_r)] \quad (4)$$

From eq. (3)- eq. (4), we have:

$$G_i^0(T) = G_i^0(T_r) + H_i^0(T) - H_i^0(T_r) - TS_i^0(T) + T_r S_i^0(T_r) \quad (5)$$

where $H_i^0(T)$ and $S_i^0(T)$ can be obtained through Shomate equations:

$$H_i^0(T) - H_i^0(T_r) = A_i t + \frac{B_i}{2} t^2 + \frac{C_i}{3} t^3 + \frac{D_i}{4} t^4 - \frac{E_i}{t} + F_i - H_i \quad (6)$$

and

$$S_i^0(T) = A_i \ln t + B_i t + \frac{C_i}{2} t^2 + \frac{D_i}{3} t^3 - \frac{E_i}{2t^2} + G_i \quad (7)$$

where $t = \frac{T[K]}{1000}$, and $A_i, B_i, C_i, D_i, E_i, F_i, G_i$ and H_i are experimentally derived constants for each molecular species i which are obtained from the National Institute of Standards and Technology (NIST) database and listed in Table S3.

For $G_i^0(T_r)$, we have:

$$\Delta G_{f,H_2O(l)}^0(T_r) = G_{H_2O(l)}^0(T_r) - G_{H_2(g)}^0(T_r) - \frac{1}{2}G_{O_2(g)}^0(T_r) \quad (8)$$

where $\Delta G_{f,H_2O(l)}^0(T_r)$ denotes the standard free energy of the formation of $H_2O(l)$ at $T=T_r=298.15$ K and it is directly obtained from the NIST database.

Combine eq. (1) ~ eq. (8) and the parameters from NIST database, we can obtain the relationship between E^0 and T :

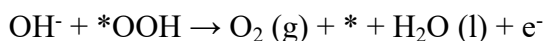
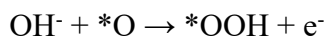
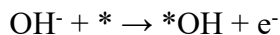
$$E_0(T) = \frac{-532.488t + 772.386t^2 - 539.463t^3 + 207.957t^4 - 252.333t \ln t + \frac{2.00879}{t} + 242.115}{2 \times 96485.33 \times 10^{-3}} \quad (9)$$

where $t = \frac{T[K]}{1000}$.

The standard potential for water splitting reaction was plotted as a function of temperature in Fig. S22 according to eq. (9). It is very close to a linear relationship ($R^2=0.9998$) with a slope of $-0.8104 \text{ mV K}^{-1}$ in the range of $273 \text{ K} \sim 473 \text{ K}$.

Supplementary Note 2: Detailed information for DFT calculation

The traditional OER mechanism is developed by Nørskov^{13, 14} including four one-electron processes:

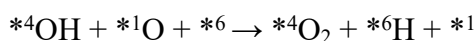
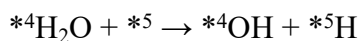
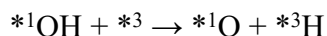
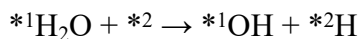
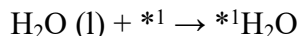


Here, * denotes the active site on the surface, (l) and (g) refer to liquid and gas phases, respectively. The free energy change (ΔG) of the reactions was calculated as follows:

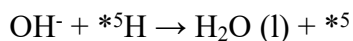
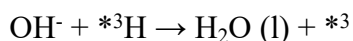
$$\Delta G = \Delta E + \Delta E_{\text{ZPE}} - T\Delta S - eU$$

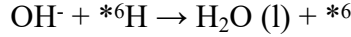
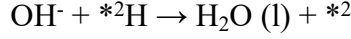
where ΔE is the total energy change of the reaction, ΔE_{ZPE} is the zero-point energy change, and ΔS is the entropy change.

The SET-OER consists of two parts: the thermal decomposition ($2\text{H}_2\text{O} \rightarrow \text{O}_2 + 4*\text{H}$) and proton-coupled electron transfer for H desorption ($4*\text{H} + 4\text{OH}^- \rightarrow 4\text{H}_2\text{O} + 4\text{e}^-$). On NiOOH (100), the elementary reactions involved in thermal decomposition are depicted in the following:

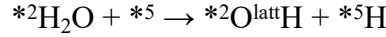
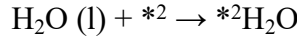
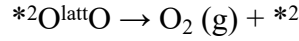
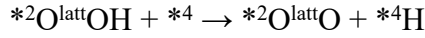
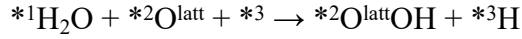
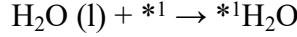


All the elementary reactions involved in H desorption can be expressed as follows:

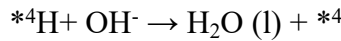
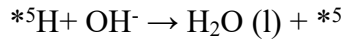
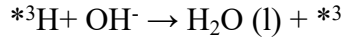
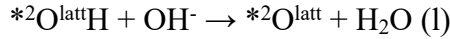




On NiOOH (001), the barrier of $*^4\text{OH} + *^1\text{O} + *^6 \rightarrow *^4\text{O}_2 + *^6\text{H} + *^1$ (1.59 eV) indicates that the reaction is unfavorable. Therefore, the assistance of the lattice O atom (O^{latt}) is required during the thermal decomposition. The elementary reactions are as follows:



And the ones of H desorption are as follows:



where $*^i$ denotes the i th site on the surface.

To compare the reaction rates of each of the above elementary reactions, their reaction barriers were calculated. For the thermal decomposition, the climbing image nudged elastic band (CI-NEB) method was employed to identify the saddle points and minimum energy paths between the stable states. For the H desorption and traditional OER mechanism which both involve the proton-coupled electron transfer, the standard Gibbs free energy of activation (ΔG^\ddagger) is estimated using Marcus theory of electron transfer¹⁵:

$$\Delta G^\ddagger (T, U) = \frac{\lambda_i}{4} \left(1 + \frac{eE_{\text{red},i,\text{RHE}}(T, 0) - eU + \Delta w_i}{\lambda_i} \right)^2$$

where λ_i and Δw_i are the reorganization free energy and the net (product minus reactant) work term, respectively. $E_{\text{red},i,\text{RHE}}^0(T, 0)$ is the standard reduction potential of the i th step at and U is applied potential referenced to the reverse hydrogen electrode (RHE). In our work, the Marcus theory parameters λ_i and Δw_i are adopted from the study by Carter et al.^{12, 16}. These parameters were fitted from the microkinetic model to obtain a good agreement with the experimental polarization curves of β -NiOOH including the K^+ and KOH concentrations. From the reaction barriers, the reaction rate k is calculated as:

$$k = \frac{k_{\text{B}}T}{h} \exp\left(-\frac{\Delta G^{\ddagger}}{k_{\text{B}}T}\right)$$

where k_{B} and h are the Boltzmann constant and Planck's constant, respectively.

Supplementary Note 3: Calculations on the overall energy efficiency

When water electrolysis is performed at high temperatures, both electricity and heat are input to produce hydrogen. The energy required for hydrogen production equals the enthalpy change (ΔH) of water splitting reaction, while the minimum electricity required for hydrogen production equals the Gibbs free energy change (ΔG) of water splitting reaction.

When $T = 298.15$ K,

$$\Delta H^0 = 285.83 \text{ kJ mol}^{-1} (E_{th}^0 = \Delta H^0/nF = 1.482 \text{ V}), \Delta G^0 = 237.14 \text{ kJ mol}^{-1} (E^0 = \Delta G^0/nF = 1.229 \text{ V}).$$

When $T = 393.15$ K,

$$\Delta H^0 = 282.81 \text{ kJ mol}^{-1} (E_{th}^0 = \Delta H^0/nF = 1.466 \text{ V}), \Delta G^0 = 222.06 \text{ kJ mol}^{-1} (E^0 = \Delta G^0/nF = 1.151 \text{ V}).$$

At a current density of 100 mA cm^{-2} , the potential needed for $\text{Ni(OH)}_2/\text{NF}$ is 1.326 V (without ir-corrected). The overpotential for HER at 100 mA cm^{-2} is estimated at around 100 mV , so the $V_{cell} = 1.426 \text{ V}$ is used in the calculation of energy efficiency. The Faradaic efficiency calculated from hydrogen is 97.8% . In this situation, electricity input is calculated as:

$$q_e = \frac{nFV_{cell}}{FE(\%)} = \frac{2 \cdot 96485 \cdot 1.426}{97.8\%} \text{ J/mol } H_2 = 281.4 \text{ kJ/mol } H_2 = 39.15 \text{ kWh/Kg } H_2$$

When the voltage of water splitting is lower than E_{th}^0 , the reaction is endothermic so extra heat is needed to maintain the operating temperature:

$$\begin{aligned} q_1 &= nF \cdot (E_{th}^0 - V_{cell}) = 2 \cdot 96485 \cdot (1.466 - 1.426) \text{ J/mol } H_2 \\ &= 7.72 \text{ kJ/mol } H_2 = 1.07 \text{ kWh/Kg } H_2 \end{aligned}$$

Heating water from 25°C to 120°C also requires heat input, which can be calculated as:

$$q_2 = n(\text{mol}) \cdot \int_{298.15 \text{ K}}^{393.15 \text{ K}} C_{p,water} dT = 7.186 \text{ kJ/mol } H_2 = 1.00 \text{ kWh/Kg } H_2$$

The water splitting system operating at high temperatures requires an insulation design to reduce heat loss from heat conduction between the system and the external environment. Such insulation design is quite mature in industry so here we assume the heat loss from heat conduction is negligible with proper heat management. The heat from the cooling process of generated gases ($4.169 \text{ kJ/mol } H_2$) is considered as low-grade heat and is not included in the recoverable energy.

In summary, with the boosting of the SET-OER, when operating at 120°C with a current density of 100 mA cm^{-2} , the required heat input = $1.07 + 1.00 \text{ kWh/kg } H_2 = 2.07 \text{ kWh/kg } H_2$ and

the required electricity input = 39.15 kWh/kg H₂. The overall energy efficiency = $39.7 / (2.07 + 39.15) * 100\% = 96.3\%$.

Supplementary Figures

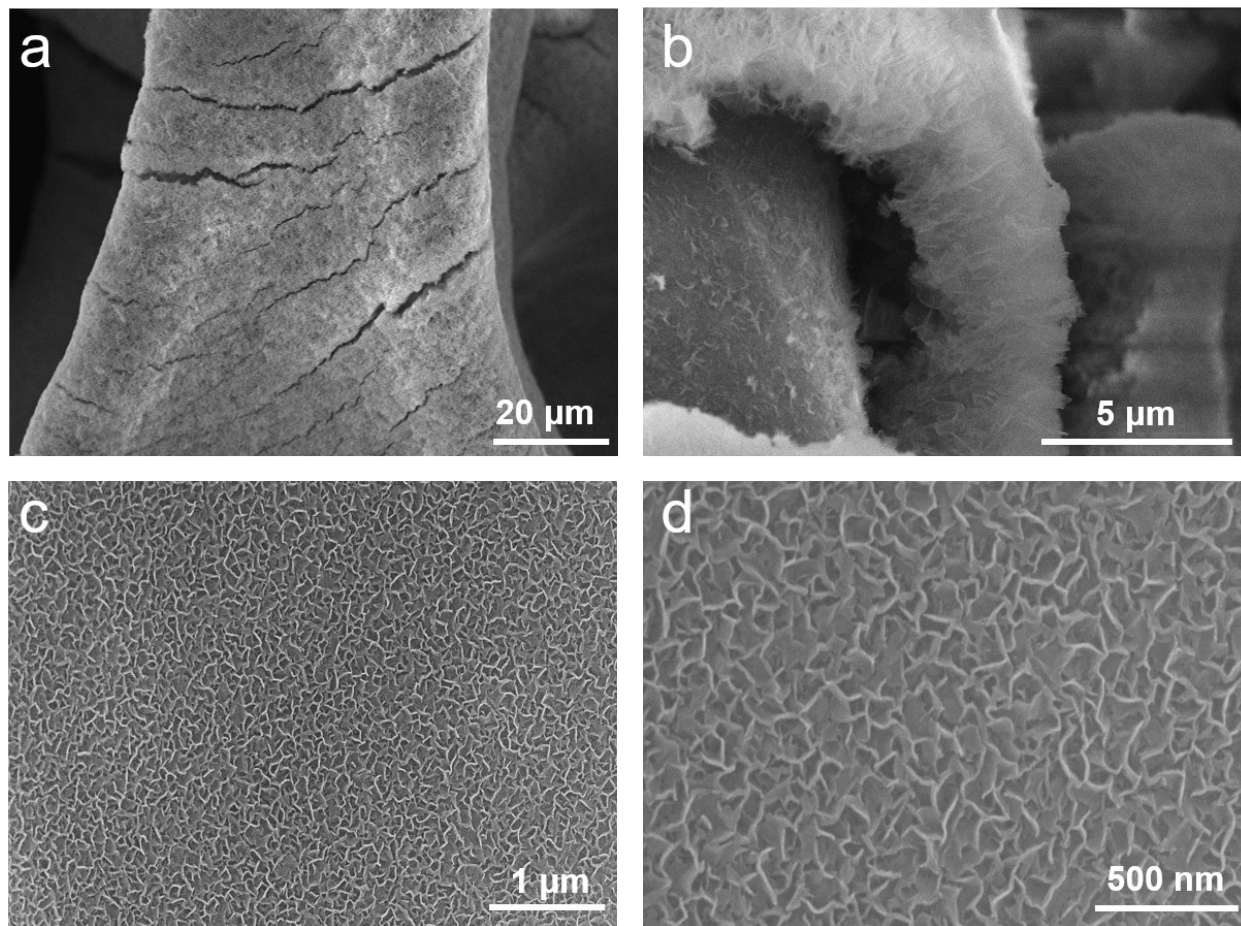


Fig. S1. SEM images of pristine Ni(OH)₂/NF at different magnifications.

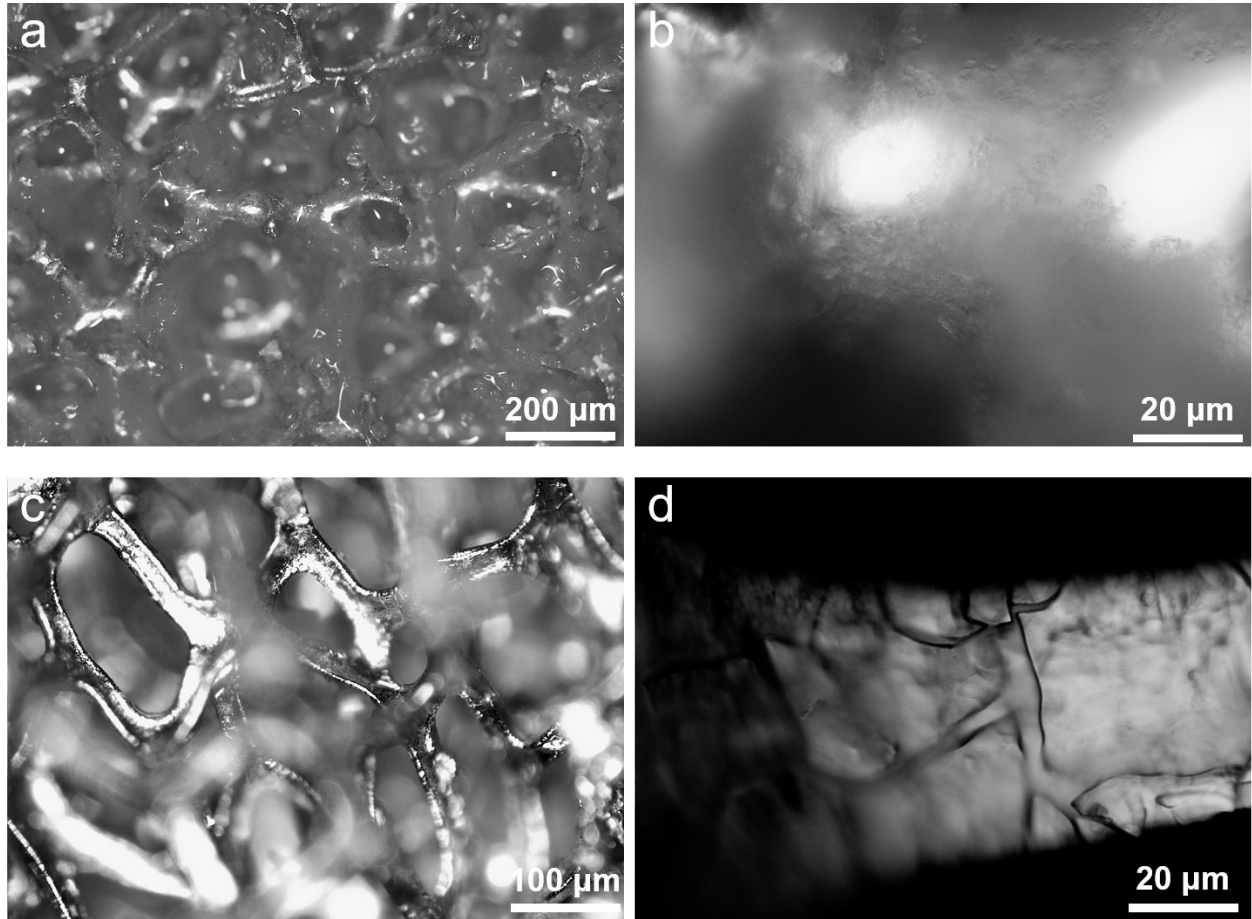


Fig. S2. Optical micrographs of the $\text{Ni}(\text{OH})_2/\text{NF}$ electrode (a-b) before SEM imaging and (c-d) after SEM imaging. No cracks were observed before the SEM imaging while cracks were distinctly observed after the SEM imaging, indicating that the cracks shown in SEM images were formed due to drying of the electrode under the high vacuum conditions inside the SEM.

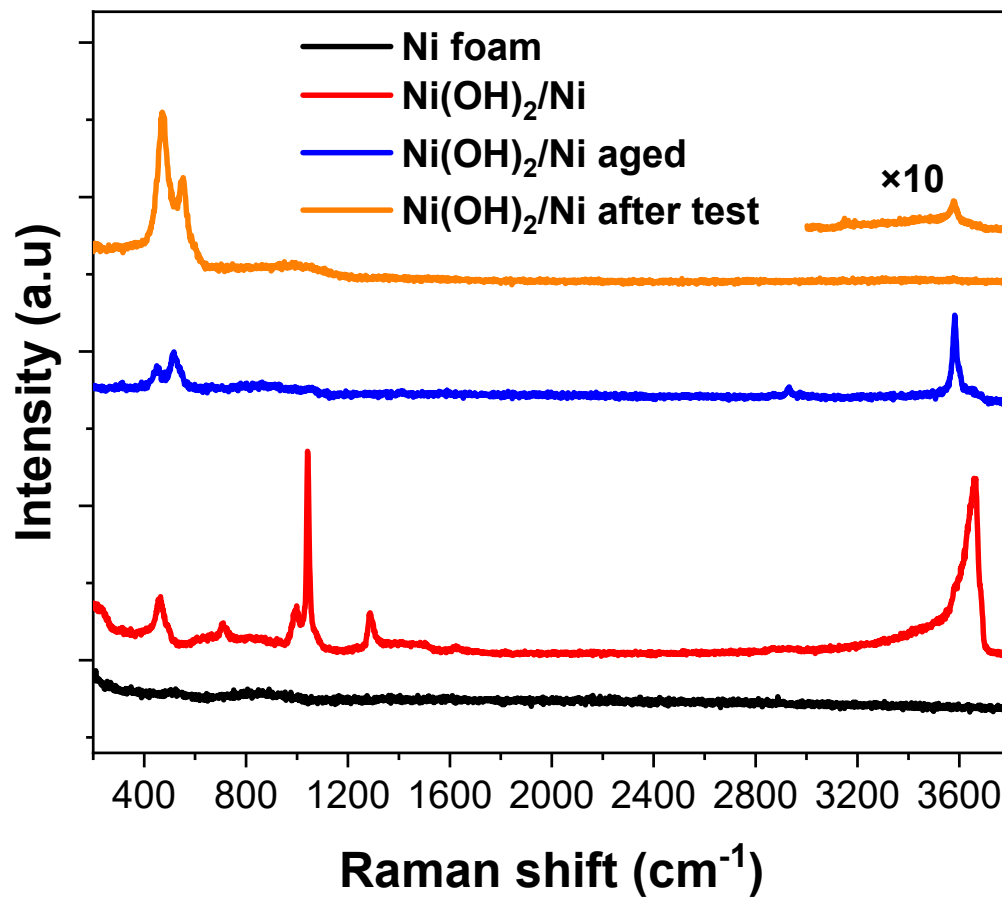


Fig. S3. Raman spectra of Ni foam, pristine Ni(OH)₂/NF, aged Ni(OH)₂/NF, and Ni(OH)₂/NF after OER stability test for 15h.

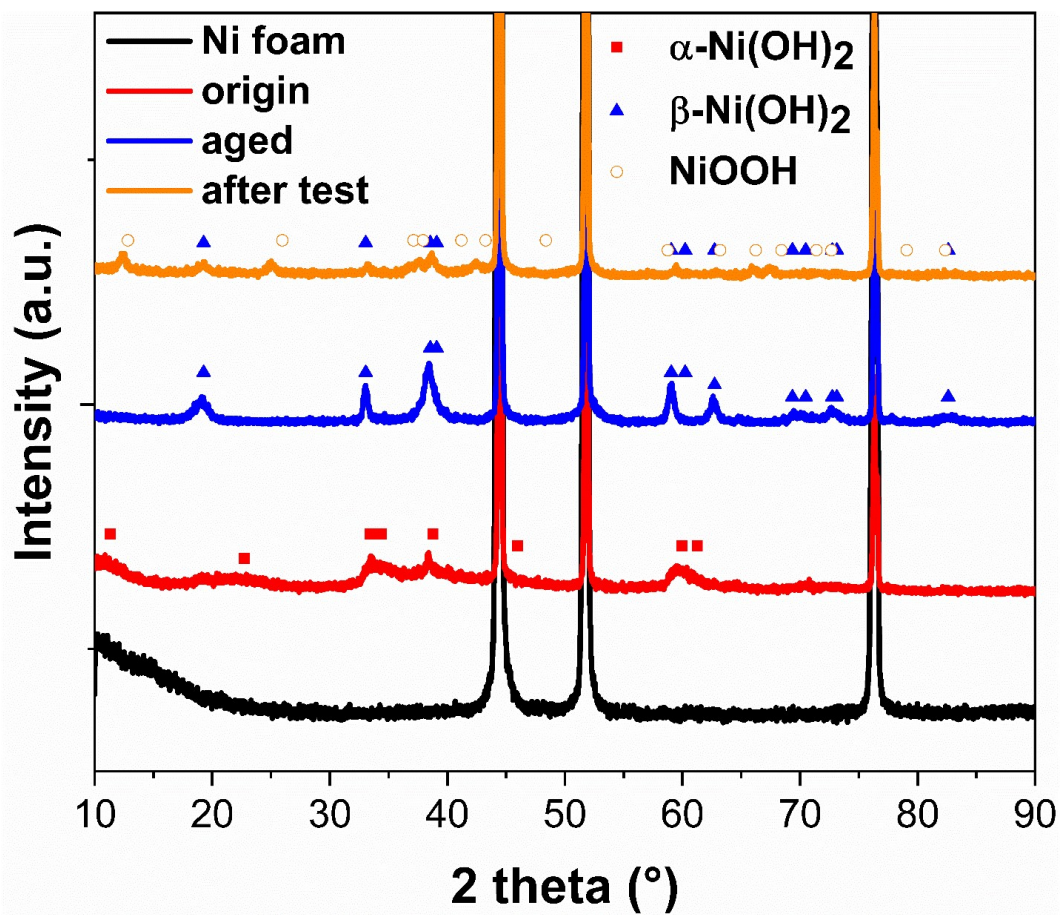


Fig. S4. XRD pattern of Ni foam, pristine Ni(OH)₂/NF, aged Ni(OH)₂/NF, and Ni(OH)₂/NF after OER stability test for 15h.

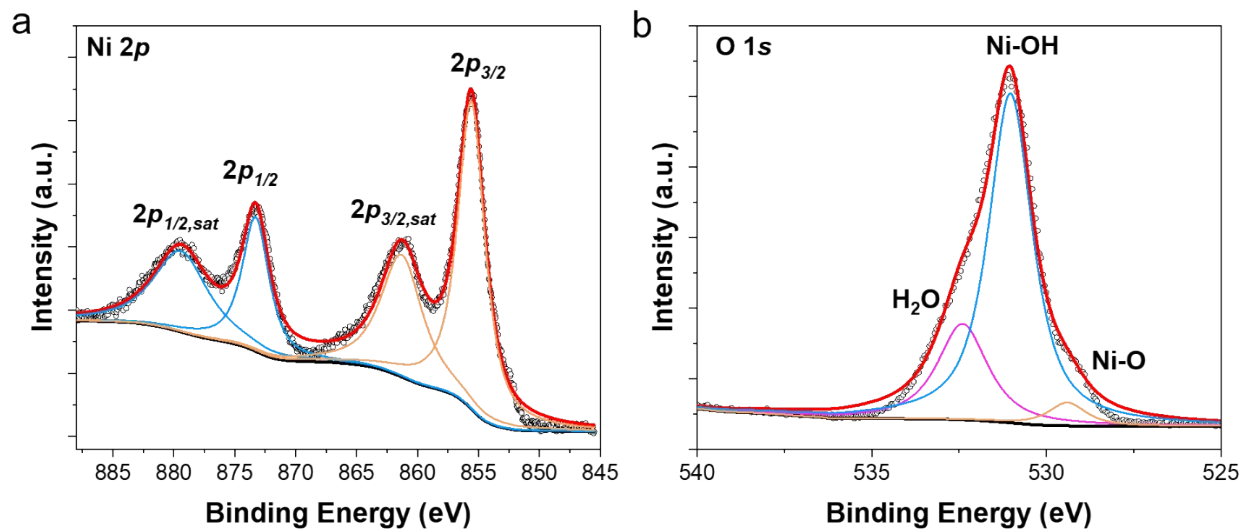


Fig. S5. XPS spectra of pristine Ni(OH)₂/Ni. (a) Ni 2p (b) O 1s.

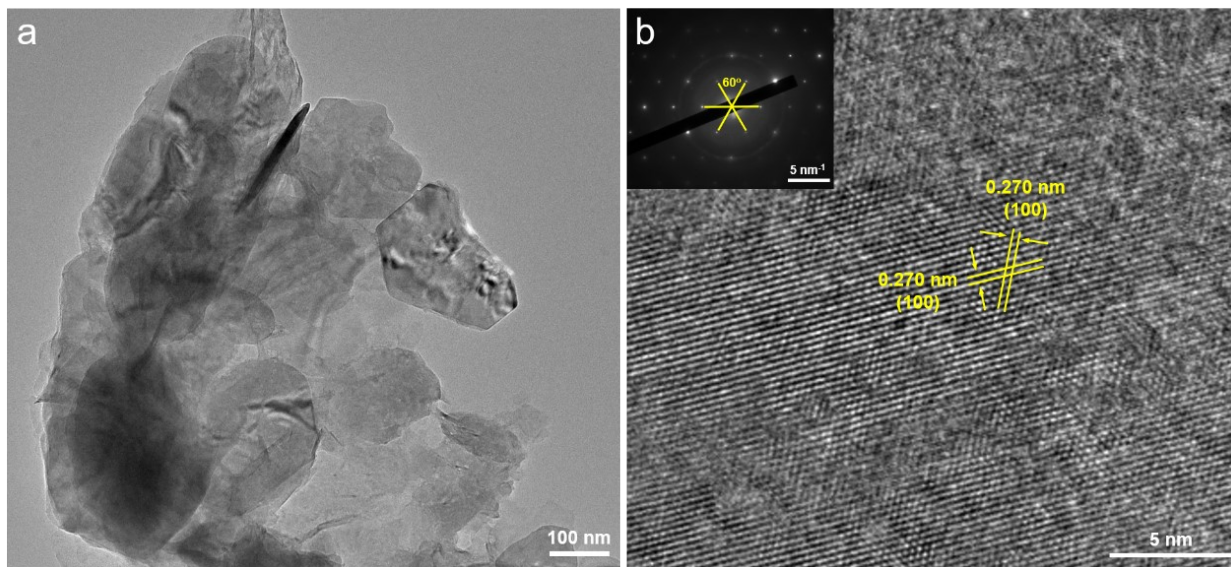


Fig. S6. TEM images of Ni(OH)₂/NF after aging in 12 Mol kg⁻¹ KOH at 120°C for 1h. (a) Low-magnification TEM image. (b) HR-TEM image. The inset shows a SAED pattern. The lattice fringes of 0.270 nm correspond to the (100) plane of β-Ni(OH)₂.

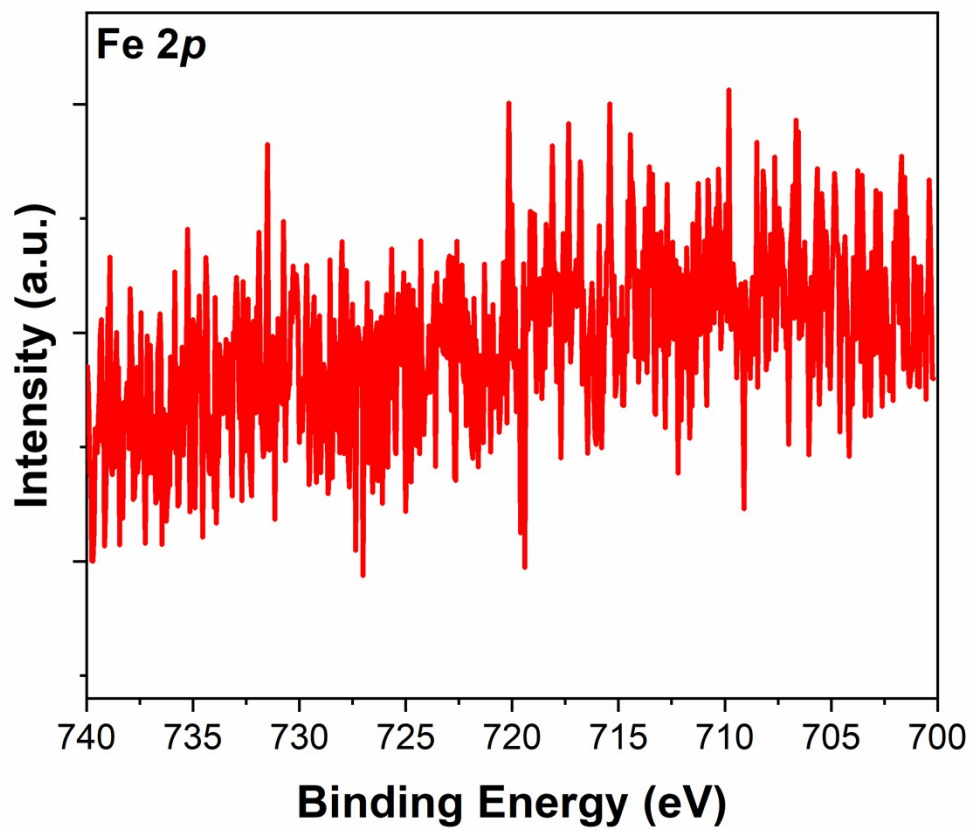


Fig. S7. Fe 2p XPS spectrum of aged Ni(OH)₂/NF electrode.

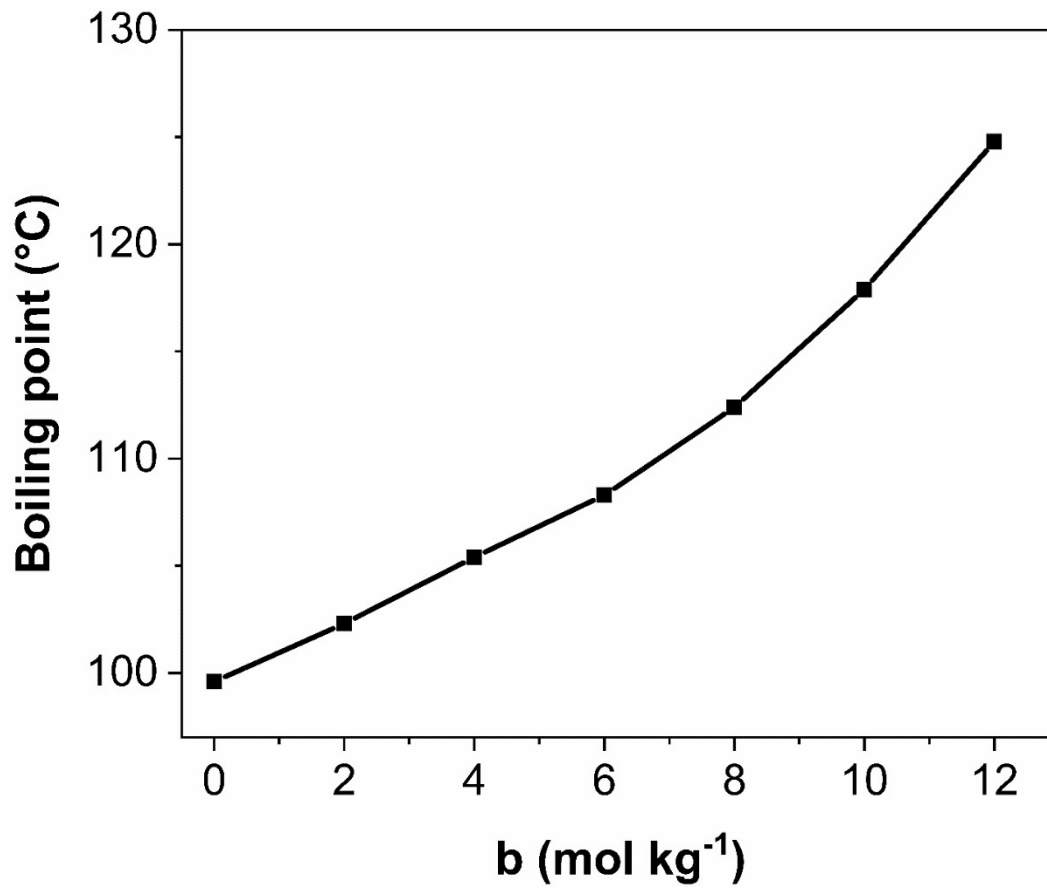


Fig. S8. Boiling point of KOH solution as a function of molality.

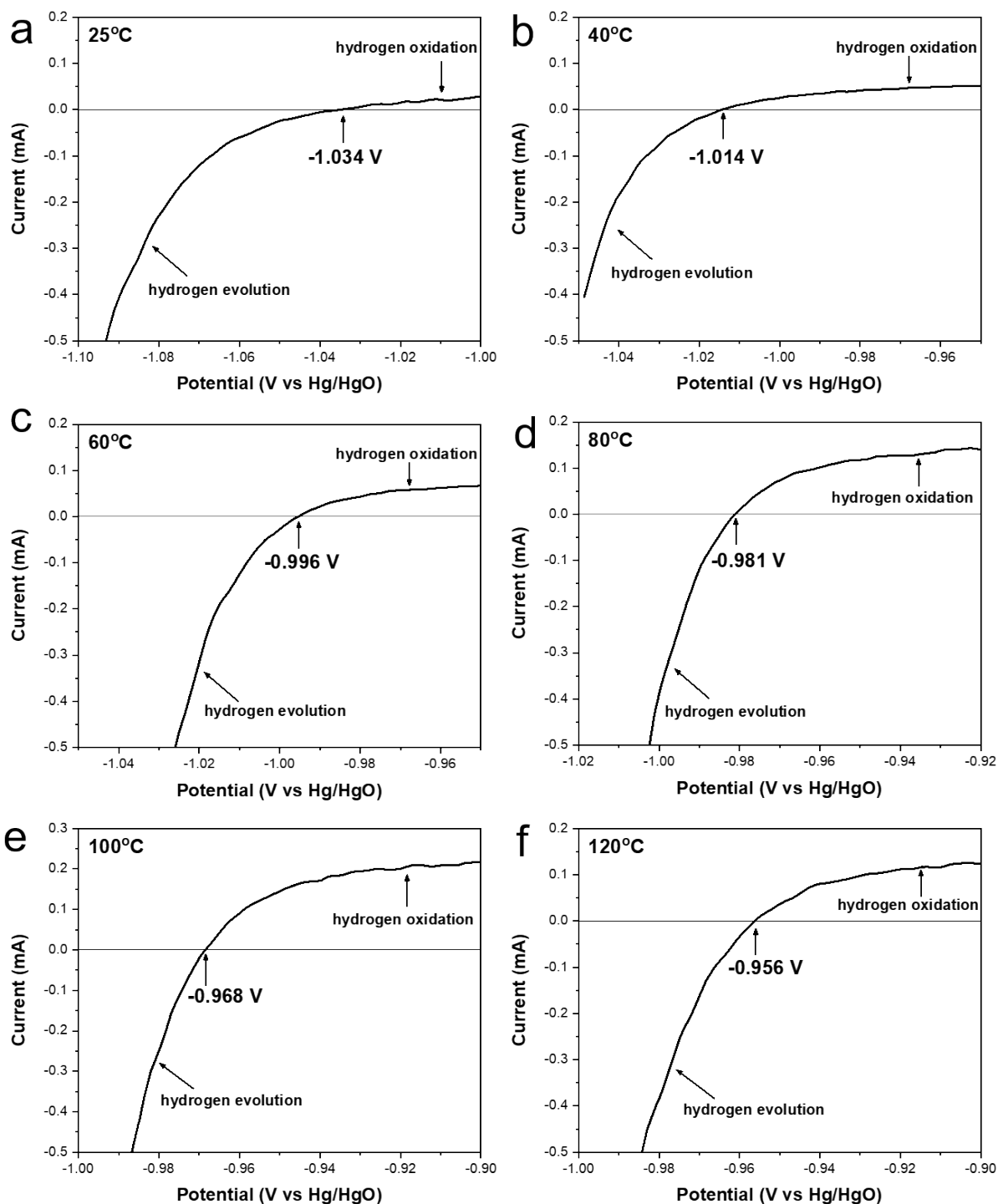


Fig. S9. RHE calibration of Hg/HgO/1M KOH reference electrode. (a-f) The LSV curves collected at (a) 25 °C, (b) 40 °C, (c) 60 °C, (d) 80 °C, (e) 100 °C, (f) 120 °C, respectively. The potential of zero current point is taken to be the thermodynamic potential (vs. Hg/HgO/1M KOH) for the hydrogen electrode reactions.

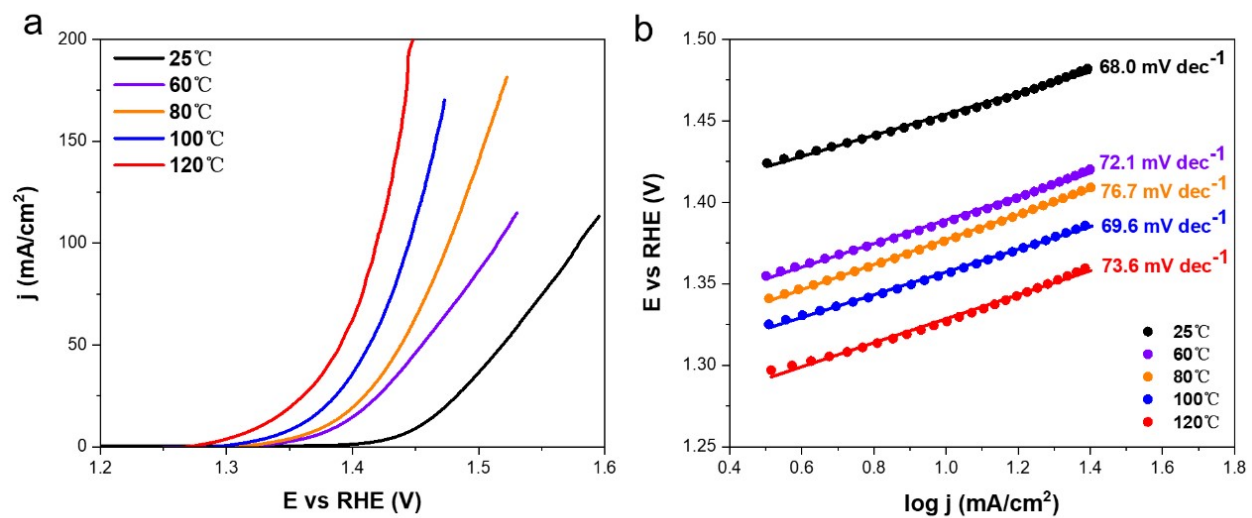


Fig. S10. (a) LSV curves at 5 mV/s and (b) corresponding Tafel slopes for commercial Ir/C from 25 °C to 120 °C.

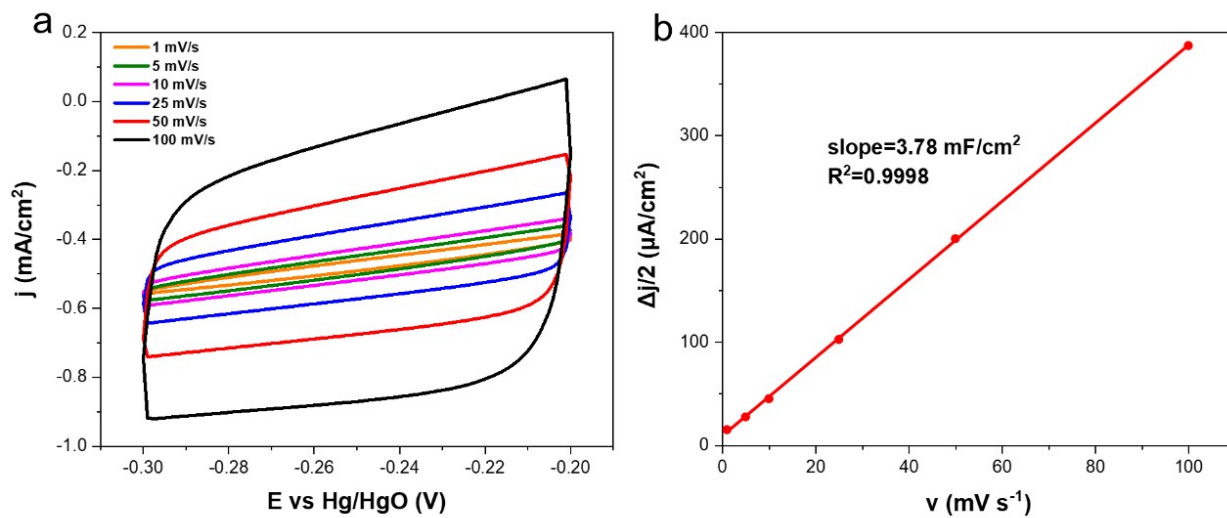


Fig. S11. (a) Cyclic voltammetry polarization curves collected in the non-faradaic potential (-0.3 ~ -0.2 V vs Hg/HgO) at various scan rates (1, 5, 10, 25, 50, and 100 mV s⁻¹). (b) The half currents difference at -0.25 V vs Hg/HgO plotted as a function of scan rate.

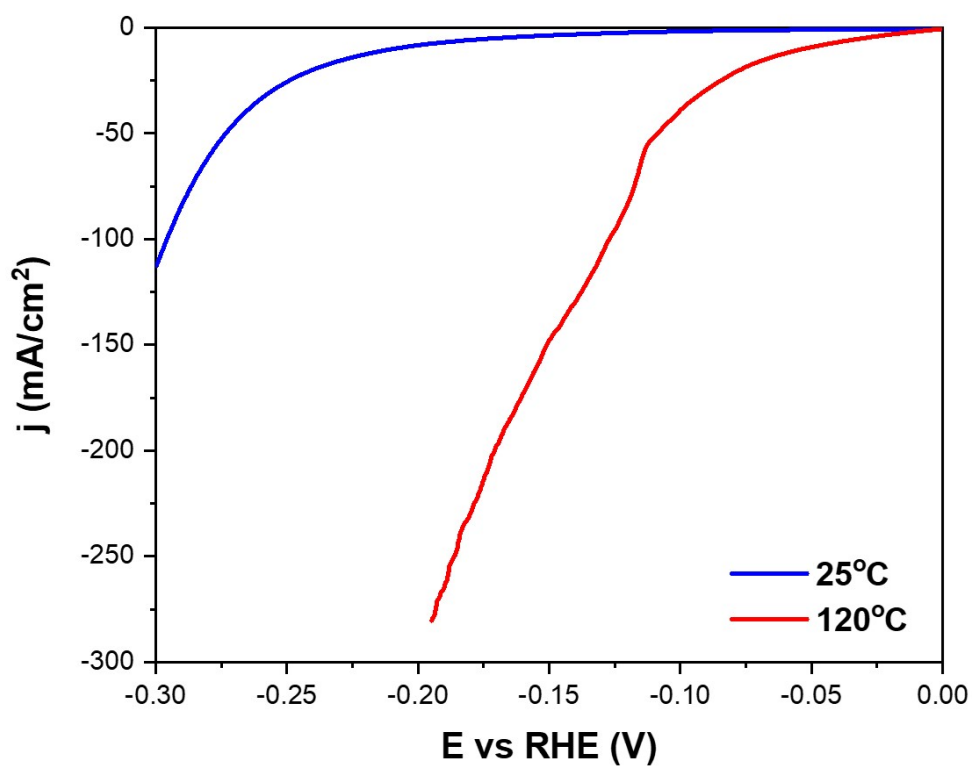


Fig. S12. HER performance of commercial Ni foam with a scan rate of 5 mV/s.

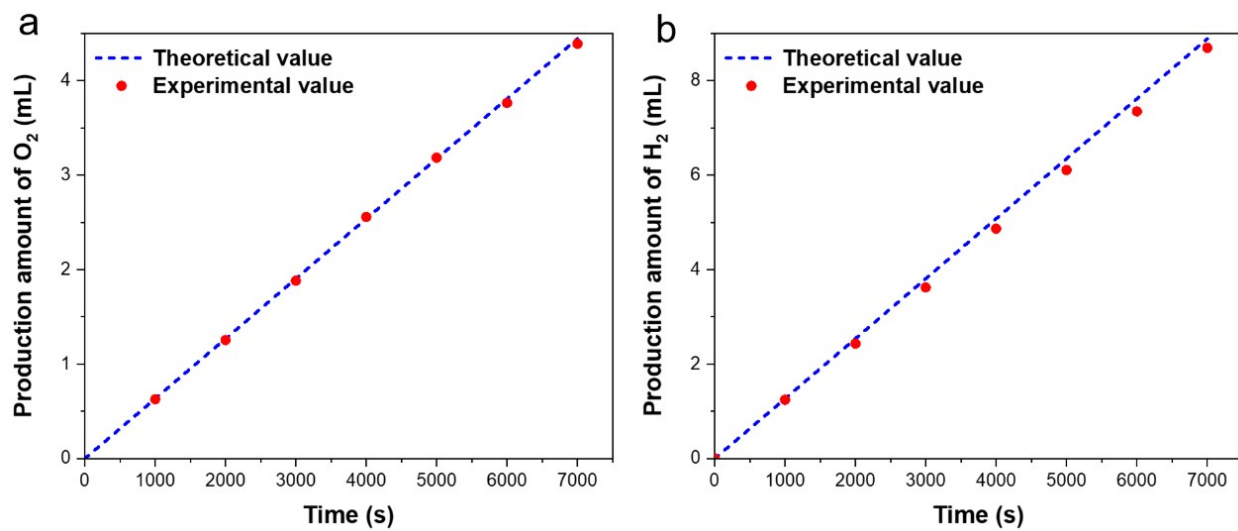


Fig. S13. Time-dependent yield of (a) O₂ and (b) H₂ measured at a current density of 10 mA cm⁻² via drainage gas gathering method.

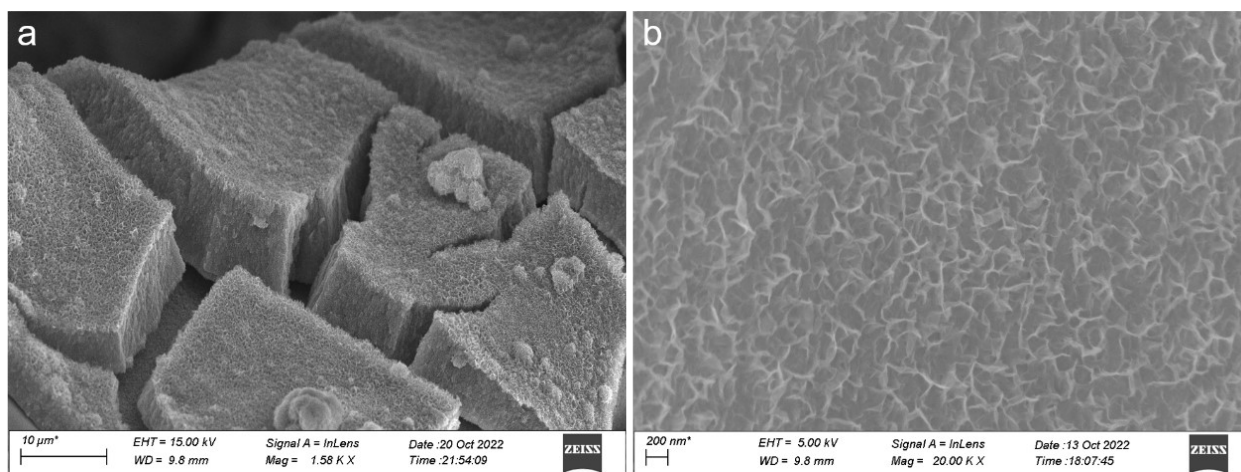


Fig. S14. SEM images of Ni(OH)₂/NF after stability test (chronopotentiometry at 10 mA cm⁻²) at different magnifications.

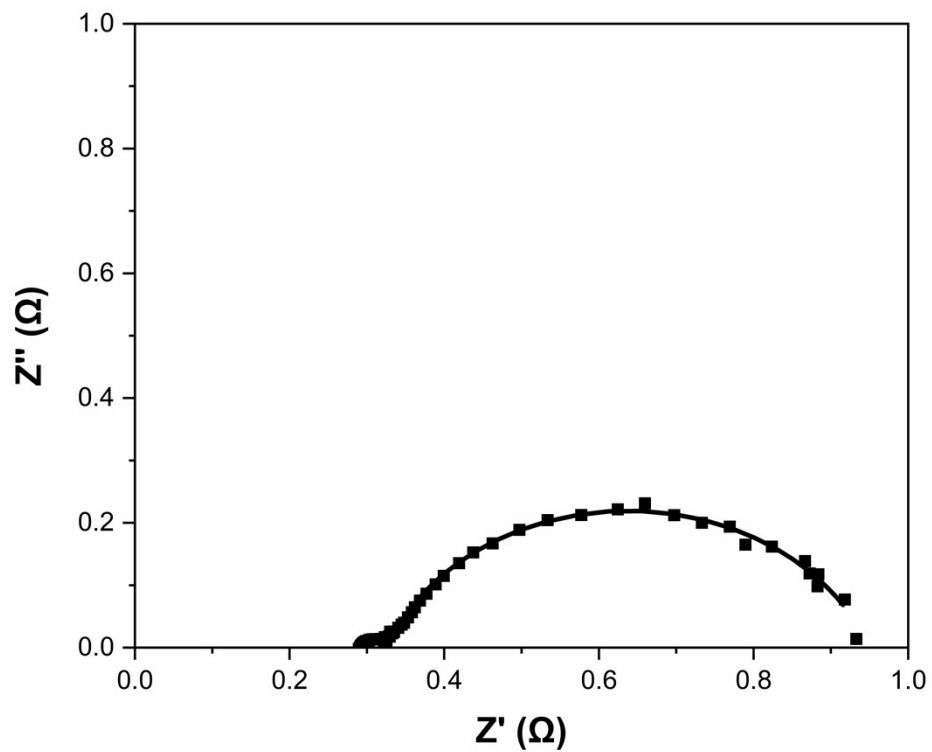


Fig. S15. EIS of Ni(OH)₂/NF at 120 °C after the long-term stability test (10 mA cm⁻² for 15h).

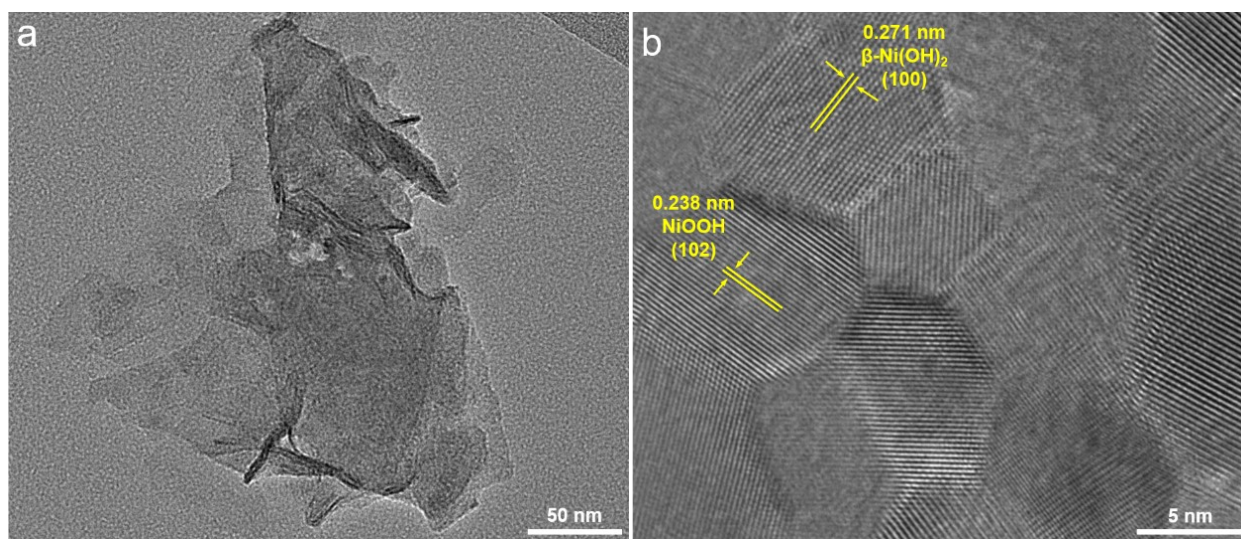
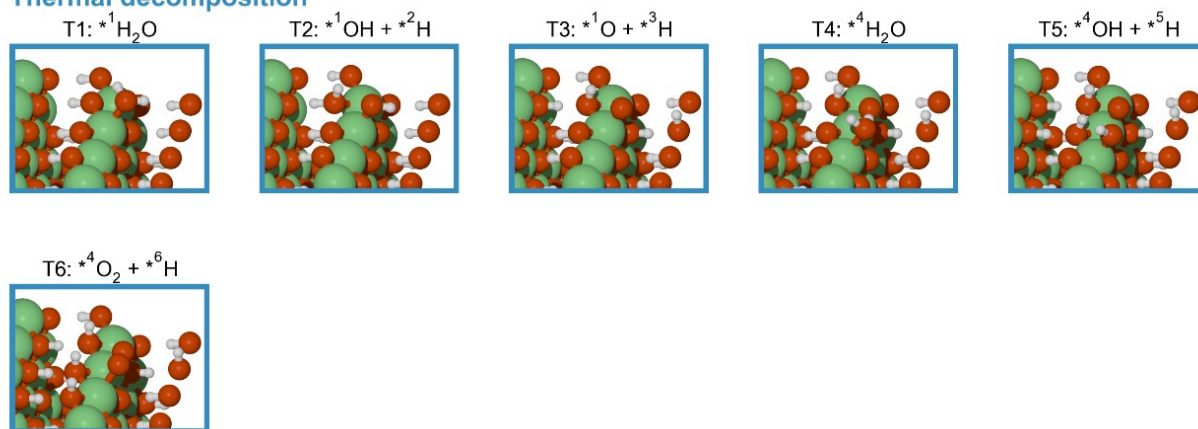
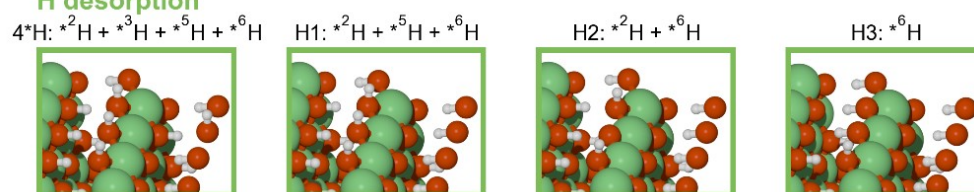


Fig. S16. TEM images of Ni(OH)₂/NF after stability test. (a) Low-magnification TEM image. (b) HR-TEM image. The lattice fringes of 0.272 nm and 0.238 nm correspond to the (100) plane of β -Ni(OH)₂ and the (102) plane of NiOOH.

Thermal decomposition



H desorption



Traditional $4e^-$ -OER

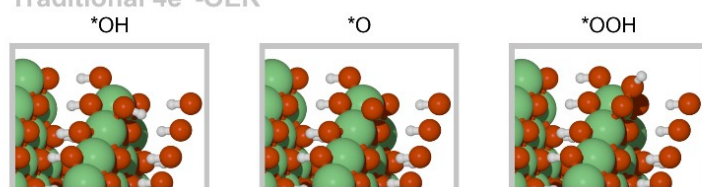


Fig. S17. The atomic structures of intermediates involved in the thermal decomposition (blue), H desorption (green), and traditional OER steps (gray) on NiOOH(100).

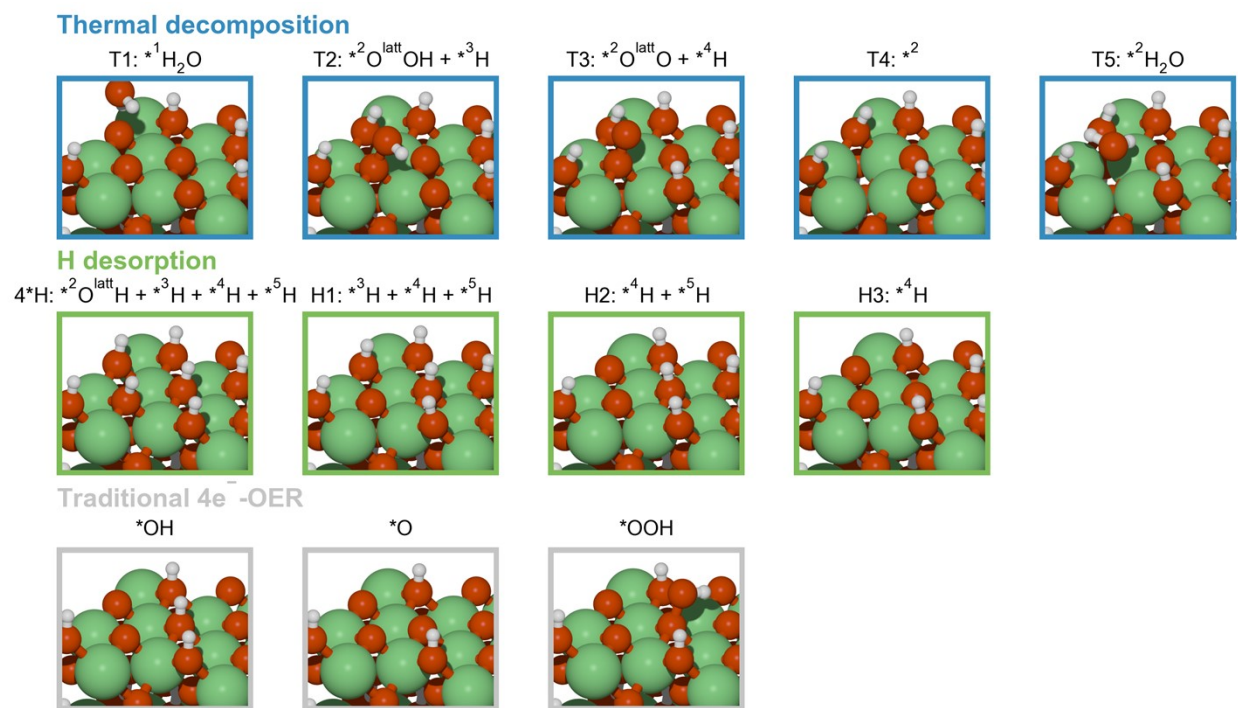


Fig. S18. The atomic structures of intermediates involved in the thermal decomposition (blue), H desorption (green), and traditional OER steps (gray) on NiOOH(001).

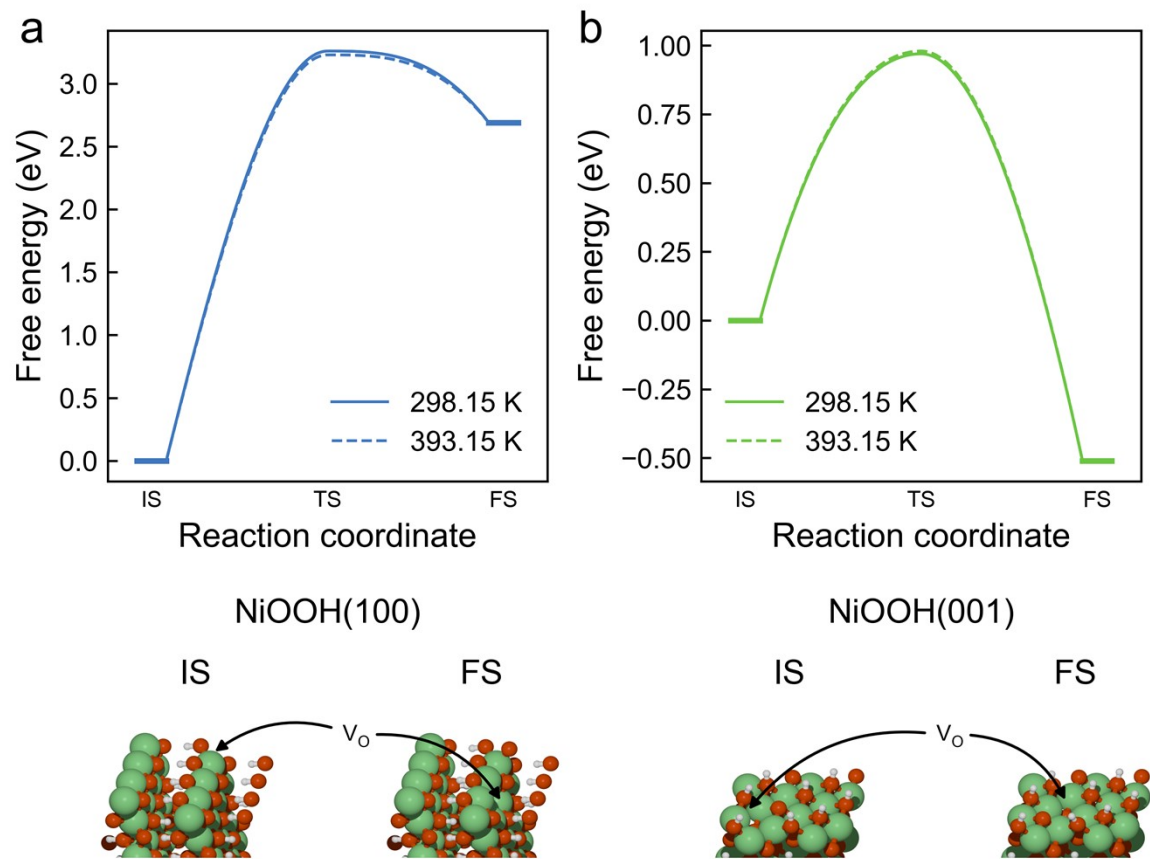


Fig. S19. The free energy diagram of the oxygen defect mobility on (a) NiOOH (100) and (b) NiOOH (001) at $T = 298.15$ (solid line) and 393.15 K (dashed line), respectively. VO represents the oxygen vacancy.”

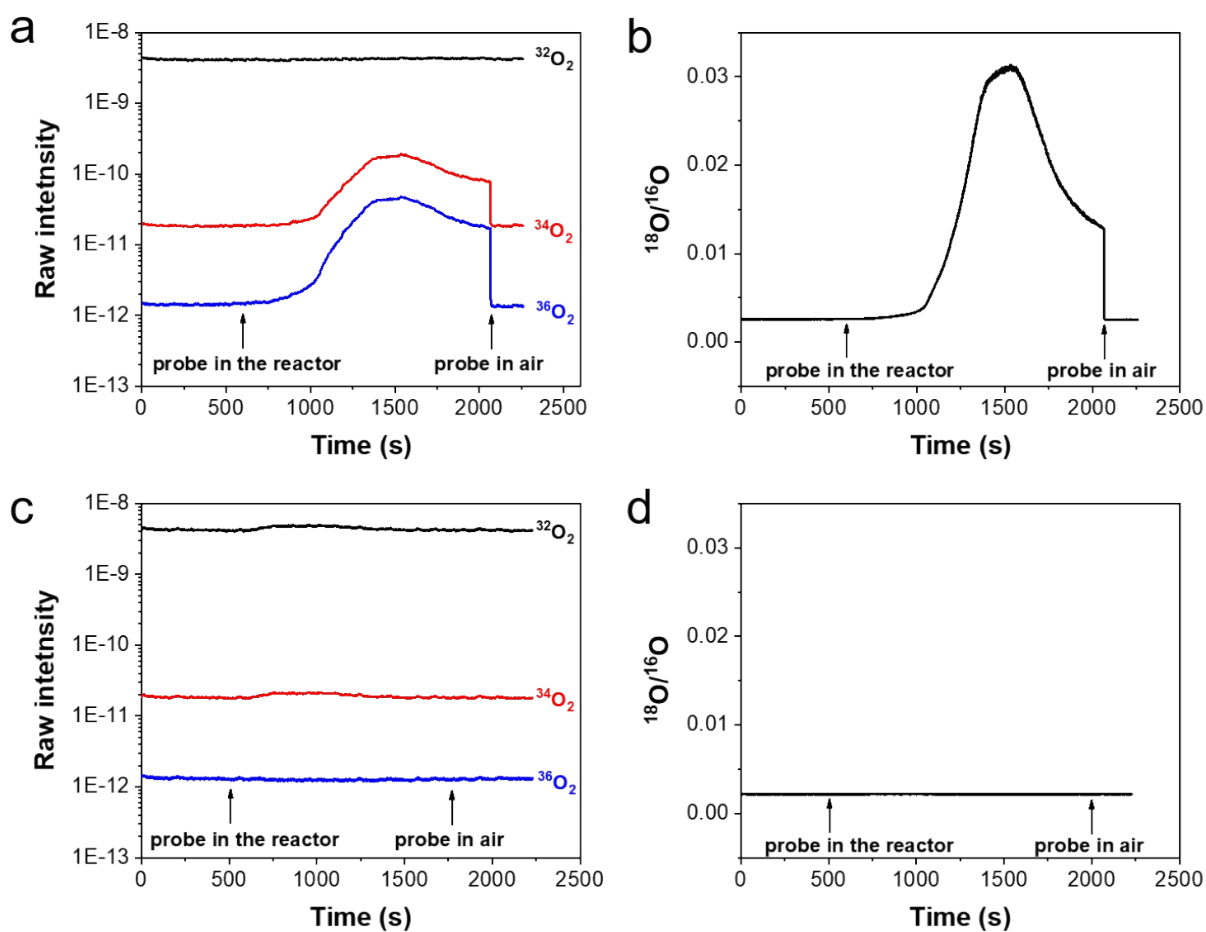


Fig. S20. (a) On-line mass spectrometry data during the thermal decomposition step with unlabeled NiOOH in ^{18}O -labeled KOH electrolyte. (b) $^{18}\text{O}/^{16}\text{O}$ ratio calculated from (a). (c) On-line mass spectrometry data during the thermal decomposition step with ^{18}O -labeled NiOOH in unlabeled KOH electrolyte. (d) $^{18}\text{O}/^{16}\text{O}$ ratio calculated from (c).

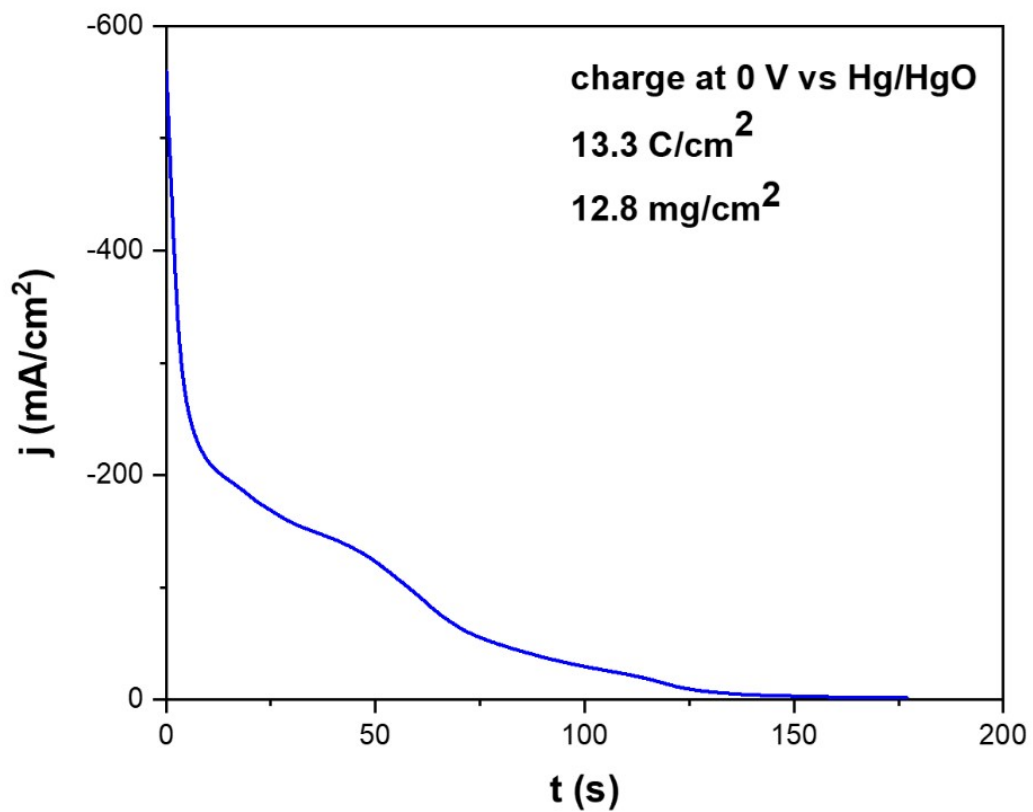


Fig. S21. Chronoamperometric curve at 0 V vs Hg/HgO under room temperature. The Ni(OH)₂/NF electrode was fully charged to NiOOH state beforehand. The current integral is used to estimate the effective Ni(OH)₂ loading of the Ni(OH)₂/NF electrode.

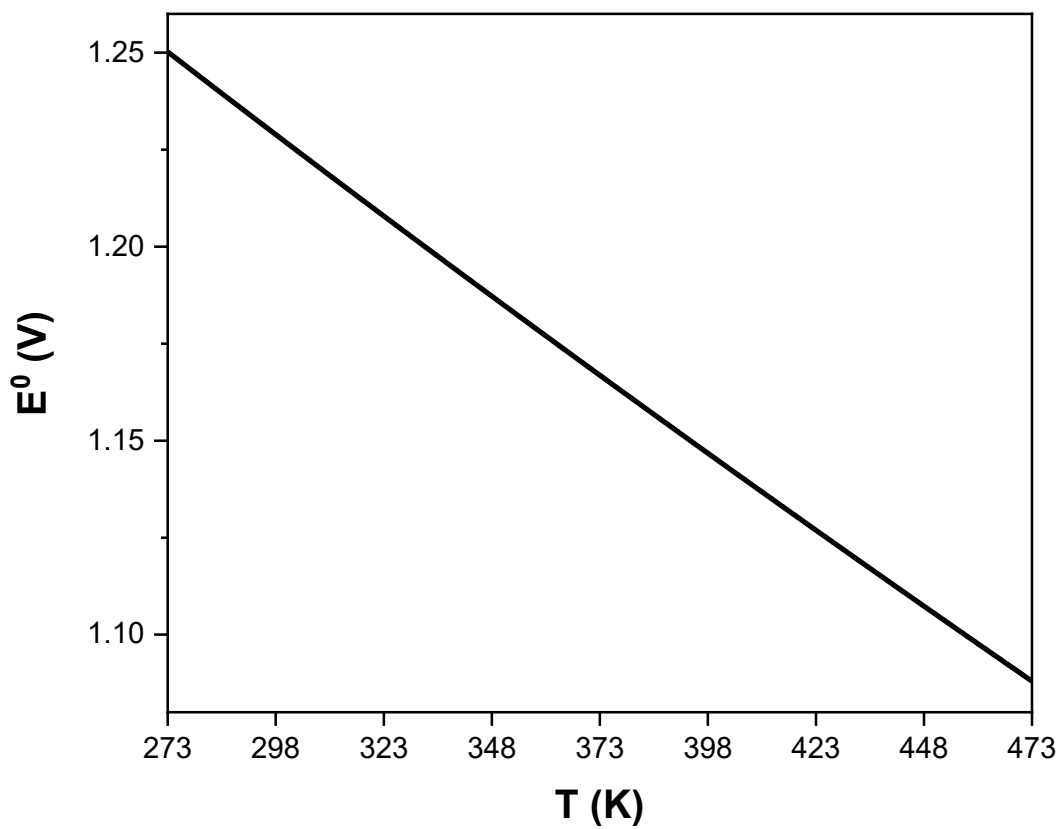


Fig. S22. The calculated standard potential for water splitting reaction as a function of temperature.

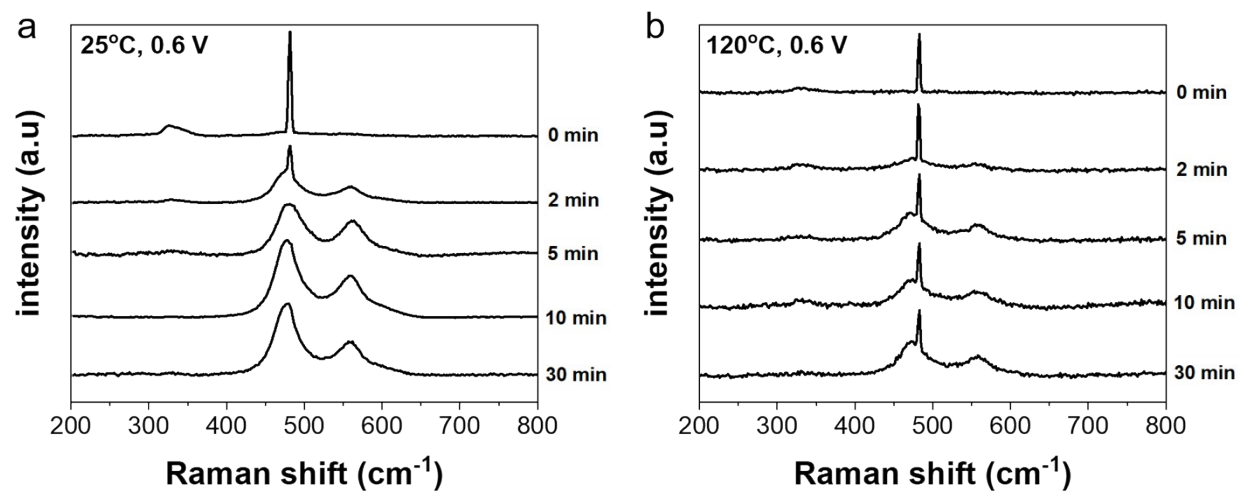


Fig. S23. *In situ* Raman spectra of Ni(OH)₂/NF electrode as a function of time when applied with a potential of 0.6 V vs Hg/HgO at (a) 25°C and (b) 120 °C.

Supplementary Tables

Table S1. Fe content of 12 mol kg⁻¹ KOH and aged Ni(OH)₂/NF electrode measured by ICP-OES.

sample	Fe content (ppm)
12 mol kg ⁻¹ KOH	< 0.5 (lower than the detection limit)
aged Ni(OH) ₂ /NF	< 20 (lower than the detection limit)

Table S2. Thermodynamic potential vs Hg/HgO for the hydrogen electrode reactions as a function of temperature.

T/°C	thermodynamic potential vs Hg/HgO for the hydrogen electrode reactions/ V
25	-1.034
40	-1.014
60	-0.996
80	-0.981
100	-0.968
120	-0.956

Table S3. Shomate equation parameters for O₂(g), H₂(g) and H₂O(l)¹⁷.

Parameter	O ₂ (g)	H ₂ (g)	H ₂ O(l)
A	31.32234	33.066178	-203.606
B	-20.23531	-11.363417	1523.29
C	57.86644	11.432816	-3196.413
D	-36.50624	-2.772874	2474.455
E	-0.007374	-0.158558	3.855326
F	-8.903471	-9.980797	-256.5478
G	246.7945	172.707974	-488.7163
H	0	0	-285.8304

Table S4. Optimum fit parameters of the EIS data in Fig. 2e to the equivalent circuit.

Temperature (°C)	R_s (Ω)	R_f (Ω)	R_{ct} (Ω)
25	0.770	0.350	2.02
120	0.258	0.035	0.756

Table S5. Comparison of the Ni(OH)₂/NF with other reported OER catalysts in the performance towards water oxidation.

Catalyst	Operating temperature (°C)	electrolyte	η (mV) @ 10 mA cm ⁻²	reference
Ni(OH) ₂ /NF	120	12 m kg ⁻¹ KOH	100	This work
NiFe LDH/NiS	RT	1M KOH	230	18
Ir _{18 wt %} -NiO	RT	1M KOH	215	19
Ir ₁ @Co/NC	RT	1M KOH	260	20
Ir/Ni(OH) ₂	RT	1M KOH	224	21
MoNiFe-27%	RT	1M KOH	242	22
Ir ₁ /CoOOH _{sur}	RT	1M KOH	210	23
Ni/Ni(OH) ₂	RT	1M KOH	270	24
Fe _{MOFs} -SO ₃	50	1M KOH	195	25
CoN	65	1M KOH	242	26
NiFeO _x /NF	72.85	1M NaOH	230	9
NiO _x (OH) _y	90	1M KOH	184	27
DR-NiOOH	52.8	1M KOH	289	28
Fe ₂ P-Co ₂ P/CF	65	1M KOH	254	29
Fe-BHT	80	1M KOH	282	11
FeCo(OH) _x	75	1M KOH	209	30
IrO ₂	75	1M KOH	253	30

Supplementary References

1. G. Kresse and J. Hafner, *Phys. Rev. B*, 1993, **47**, 558-561.
2. G. Kresse and J. Furthmuller, *Phys. Rev. B*, 1996, **54**, 11169-11186.
3. J. P. Perdew, K. Burke and M. Ernzerhof, *Phys. Rev. Lett.*, 1996, **77**, 3865-3868.
4. H. J. Monkhorst and J. D. Pack, *Phys. Rev. B*, 1976, **13**, 5188-5192.
5. S. Grimme, *J. Comput. Chem.*, 2006, **27**, 1787-1799.
6. S. Grimme, S. Ehrlich and L. Goerigk, *J. Comput. Chem.*, 2011, **32**, 1456-1465.
7. M. Cococcioni and S. de Gironcoli, *Phys. Rev. B*, 2005, **71**.
8. Q. Hu, Y. F. Xue, J. X. Kang, I. Scivetti, G. Teobaldi, A. Selloni, L. Guo and L. M. Liu, *Acs Catal.*, 2022, **12**, 295-304.
9. E. Nurlaela, T. Shinagawa, M. Qureshi, D. S. Dhawale and K. Takanae, *Acs Catal.*, 2016, **6**, 1713-1722.
10. Y. Sun, L. Yuan, Z. Y. Liu, Q. Wang, K. K. Huang and S. H. Feng, *Mater. Chem. Front.*, 2019, **3**, 1779-1785.
11. X. Fan, S. Tan, J. Yang, Y. Liu, W. Bian, F. Liao, H. Lin and Y. Li, *ACS Energy Lett.*, 2021, **7**, 343-348.
12. A. G. Rajan, J. M. P. Martirez and E. A. Carter, *ACS Catal.*, 2021, **11**, 11305-11319.
13. J. K. Norskov, J. Rossmeisl, A. Logadottir, L. Lindqvist, J. R. Kitchin, T. Bligaard and H. Jonsson, *J. Phys. Chem. B*, 2004, **108**, 17886-17892.
14. J. Rossmeisl, Z. W. Qu, H. Zhu, G. J. Kroes and J. K. Norskov, *J. Electroanal. Chem.*, 2007, **607**, 83-89.
15. R. A. Marcus, *J. Chem. Phys.*, 1965, **43**, 679-&.
16. A. G. Rajan and E. A. Carter, *Energy Environ. Sci.*, 2020, **13**, 4962-4976.
17. Chase, M.W., Jr., NIST-JANAF Thermochemical Tables, Fourth Edition, J. Phys. Chem. Ref. Data, Monograph 9, 1998, 1-1951.
18. Q. L. Wen, K. Yang, D. J. Huang, G. Cheng, X. M. Ai, Y. W. Liu, J. K. Fang, H. Q. Li, L. Yu and T. Y. Zhai, *Adv. Energy Mater.*, 2021, **11**.
19. Q. Wang, X. Huang, Z. L. Zhao, M. Wang, B. Xiang, J. Li, Z. Feng, H. Xu and M. Gu, *J. Am. Chem. Soc.*, 2020, **142**, 7425-7433.
20. W. H. Lai, L. F. Zhang, W. B. Hua, S. Indris, Z. C. Yan, Z. Hu, B. Zhang, Y. Liu, L. Wang, M. Liu, R. Liu, Y. X. Wang, J. Z. Wang, Z. Hu, H. K. Liu, S. L. Chou and S. X. Dou, *Angew. Chem. Int. Ed.*, 2019, **58**, 11868-11873.
21. G. Zhao, P. Li, N. Cheng, S. X. Dou and W. Sun, *Adv. Mater.*, 2020, **32**, e2000872.
22. Z. He, J. Zhang, Z. Gong, H. Lei, D. Zhou, N. Zhang, W. Mai, S. Zhao and Y. Chen, *Nat. Commun.*, 2022, **13**, 2191.
23. C. Feng, Z. Zhang, D. Wang, Y. Kong, J. Wei, R. Wang, P. Ma, H. Li, Z. Geng, M. Zuo, J. Bao, S. Zhou and J. Zeng, *J. Am. Chem. Soc.*, 2022, **144**, 9271-9279.
24. L. Dai, Z. N. Chen, L. Li, P. Yin, Z. Liu and H. Zhang, *Adv. Mater.*, 2020, **32**, e1906915.
25. K. Feng, D. Zhang, F. F. Liu, H. Li, J. B. Xu, Y. J. Xia, Y. Y. Li, H. P. Lin, S. Wang, M. W. Shao, Z. H. Kang and J. Zhong, *Adv. Energy Mater.*, 2020, **10**.
26. B. Jin, Y. Li, J. Wang, F. Meng, S. Cao, B. He, S. Jia, Y. Wang, Z. Li and X. Liu, *Small*, 2019, **15**, e1903847.
27. D. Liu, Y. Yang, H. Zhu, D. Liu, S. Yan and Z. Zou, *J. Phys. Chem. Lett.*, 2022, **13**, 49-57.
28. X. Liu, K. Ni, B. Wen, R. T. Guo, C. J. Niu, J. S. Meng, Q. Li, P. J. Wu, Y. W. Zhu, X. J. Wu and L. Q. Mai, *Acs Energy Lett.*, 2019, **4**, 2585-2592.

29. X. Y. Liu, Y. D. Yao, H. Zhang, L. Pan, C. X. Shi, X. W. Zhang, Z. F. Huang and J. J. Zou, *ACS Sustainable Chem. Eng.*, 2020, **8**, 17828-17838.
30. G. Zhang, H. Wang, J. Yang, Q. Zhao, L. Yang, H. Tang, C. Liu, H. Chen, Y. Lin and F. Pan, *Inorg. Chem.*, 2018, **57**, 2766-2772.